chemosensors

MDPI

*Article*

# Label-Free $ZnIn_2S_4$/UiO-66-$NH_2$ Modified Glassy Carbon Electrode for Electrochemically Assessing Fish Freshness by Monitoring Xanthine and Hypoxanthine

**Debin Song [1,†], Qiaowei Chen [1,2,†], Chunyang Zhai [2], Hengcong Tao [1], Lina Zhang [1,2], Tianbo Jia [1], Zhiwang Lu [1], Wuyang Sun [1], Pengxiang Yuan [3,*] and Baikang Zhu [1,*]**

1 School of Petrochemical Engineering & Environment, Zhejiang Ocean University, Zhoushan 316022, China; 025125@zjou.edu.cn (D.S.); s19082000010@zjou.edu.cn (Q.C.); hengcongtao@zjou.edu.cn (H.T.); 2011086208@nbu.edu.cn (L.Z.); s19082000008@zjou.edu.cn (T.J.); s20082000009@zjou.edu.cn (Z.L.); 025140@zjou.edu.cn (W.S.)
2 School of Materials Science and Chemical Engineering, Ningbo University, Ningbo 315211, China; zhaichunyang@nbu.edu.cn
3 College of Food Science and Pharmacy, Zhejiang Ocean University, Zhoushan 316022, China
* Correspondence: 011107@zjou.edu.cn (P.Y.); zszbk@zjou.edu.cn (B.Z.)
† These authors contributed equally to this work.

**Abstract:** Considering that simultaneous detection of xanthine (XA) and hypoxanthine (HXA) has been proved to be a reliable and feasible method for assessing fish freshness, a novel electrochemical sensing platform based on the $ZnIn_2S_4$/UiO-66-$NH_2$ modified glassy carbon electrode (GCE) was constructed in this study for XA and HXA determination. X-ray powder diffraction (XRD), X-ray photoelectron spectroscopy (XPS), transmission electron microscopy (TEM), and Fourier transform infrared spectroscopy (FT-IR) were performed to exhibit the morphology and structural characteristics of $ZnIn_2S_4$/UiO-66-$NH_2$. The Brunauer–Emmett–Teller (BET) displayed that the introduction of UiO-66-$NH_2$ can improve the specific surface area of the hybrid. Besides, the electrochemical sensing performance of $ZnIn_2S_4$/UiO-66-$NH_2$ was evaluated by cyclic voltammetry (CV) and differential pulse voltammetry (DPV). For simultaneously detecting XA and HXA, the fabricated electrochemical sensor shows wide linear ranges (0.025–40 μM and 0.3–40 μM) with low detection limits (0.0083 μM and 0.1 μM). This sensor also has 96–103% recovery in detecting XA and HXA content in large yellow croaker meat samples, demonstrating a promising application in the marine food industry.

**Keywords:** xanthine; hypoxanthine; simultaneous detection; electrochemical sensor

check for updates

**Citation:** Song, D.; Chen, Q.; Zhai, C.; Tao, H.; Zhang, L.; Jia, T.; Lu, Z.; Sun, W.; Yuan, P.; Zhu, B. Label-Free $ZnIn_2S_4$/UiO-66-$NH_2$ Modified Glassy Carbon Electrode for Electrochemically Assessing Fish Freshness by Monitoring Xanthine and Hypoxanthine. *Chemosensors* **2022**, *10*, 158. https://doi.org/10.3390/chemosensors10050158

Academic Editor: Camelia Bala

Received: 22 March 2022
Accepted: 20 April 2022
Published: 25 April 2022

**Publisher's Note:** MDPI stays neutral with regard to jurisdictional claims in published maps and institutional affiliations.

**Copyright:** © 2022 by the authors. Licensee MDPI, Basel, Switzerland. This article is an open access article distributed under the terms and conditions of the Creative Commons Attribution (CC BY) license (https://creativecommons.org/licenses/by/4.0/).

## 1. Introduction

It is well known that fish freshness is an important evaluation index to ensure that fish can be processed healthily [1,2]. The large yellow croaker (*Pseudosciaena crocea*) is nutritious and delicious, and it is an important valuable economic fish in the world, especially in the East China Sea. However, the large yellow croaker is highly perishable, and it is difficult to evaluate its freshness level or commercial grade in a timely manner. Therefore, it is urgent to develop an efficient and low-cost evaluation method for fish. Once the fish is inactivated, adenosine triphosphate (ATP), which is an extremely important energy source in physiology, will be degraded to inosine (HxR) by various enzymes and then be enzymatically digested into hypoxanthine (HXA) and xanthine (XA); eventually it will become uric acid (UA). The detailed decomposition process of ATP is as follows: ATP → adenosine diphosphate (ADP) → adenosine monophosphate (AMP) → inosinate (IMP) → HxR → HXA → XA → UA. Therefore, HXA and XA are the dominating components which incur bitter fish, and they would accumulate over the course of time [3–5]. Moreover, a high level of HXA and XA can also cause gout, hyperuricemia, renal failure, and other diseases, which are harmful for human health [6,7]. Consequently, HXA and XA

are a trustworthy indicator of fish freshness and selected as strong indicators to assess the freshness of fish in this work.

Up to now, the detection methods for HXA and XA in the marine food industry mainly include chromatography [8], colorimetry [9], enzymatic method [10], and electrochemical methods [11–13]. Electrochemical methods stand out, relying on various strengths of simple operation, short analysis time, lower cost, high sensitivity, and low detection limit [14,15]. To enhance its wide application, the original glassy carbon electrode (GCE) is always modified. The remarkable selection of electrode modified material, it should be noted, is a winning strategy to improve the sensitivity of electrochemical detection. Recently, $ZnIn_2S_4$ has triggered extensive consideration and is largely applied in sensors thanks to its perfect chemical stability, high electrochemical selectivity, and efficient surface area [16–18]. Pourtaheri et al. [18] proposed that $ZnIn_2S_4$ NPs and an ionic liquid as a modifier be applied to fabricate a novel electrochemical sensor for sensitively sensing gliclazide and glibenclamide. To the best of our knowledge, there is no report about XA or HXA determination on a $ZnIn_2S_4$-based sensor, probably due to the insufficient adsorption capacity of $ZnIn_2S_4$ for XA and HXA molecules.

Metal organic frameworks (MOFs) can provide ample absorbed channels and active sites in favor of the contact between reactants and the active center [19–21]. Li et al. [21] designed a series of Cu-BTC frameworks with different shapes by adjusting the amount of triethylamine and demonstrated that the increase of triethylamine amount could reduce particle size and enhance particle uniformity, thereby improving the electrochemical performance and sensing property towards XA and HXA. UiO-66-$NH_2$, constructed by coordination bonds between organic ligands and metal ions, has been widely utilized in many food detecting fields due to its adjustable aperture, facile preparation, and high surface area [22,23].

In this study, we have designed the binary $ZnIn_2S_4$/UiO-66-$NH_2$ materials to construct an electrochemical sensing platform for HXA and XA simultaneously in fish. Through a variety of tests, the outcomes not only prove that this sensing platform possesses a lower detection limit and wider linear ranges but also attest to the practical application in assessing the freshness of fish.

## 2. Materials and Methods

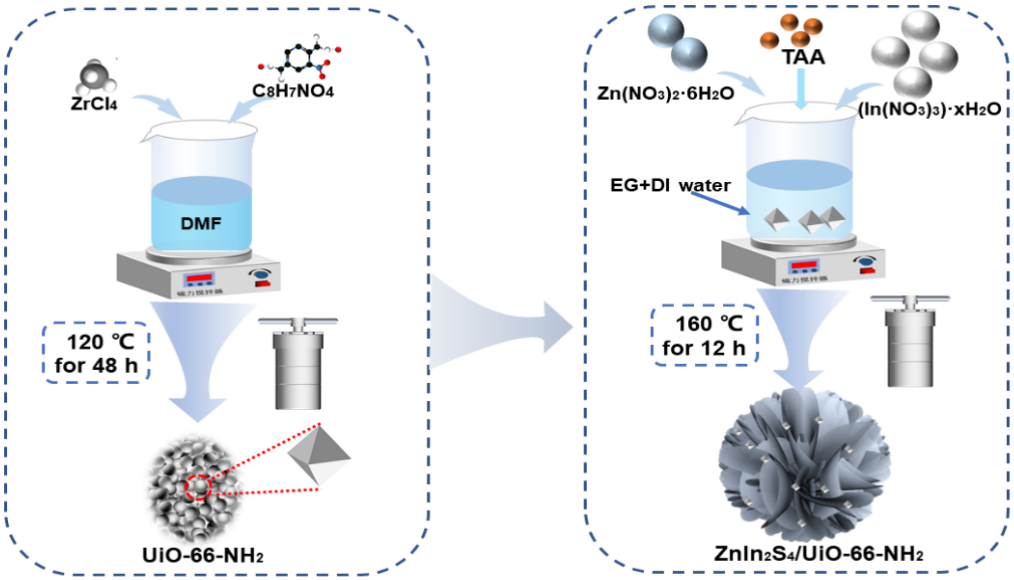
### *2.1. Materials*

Zirconium tetrachloride ($ZrCl_4$), 2-aminoterephthalic acid, dimethyl formamide (DMF), zinc nitrate hexahydrate (Zn $(NO_3)_2 \cdot 6H_2O$), indium nitrate hydrate (In $(NO_3)_3) \cdot xH_2O$, and thioacetamide (TAA) were purchased from Shanghai, China. Ethylene glycol (EG), potassium chloride (KCl), sodium dihydrogen phosphate ($NaH_2PO_4$), disodium phosphate ($Na_2HPO_4$), sodium sulfate ($Na_2SO_4$), potassium ferrocyanide and potassium ferricyanide ($K_4$[Fe $(CN)_6$]/$K_3$[Fe $(CN)_6$]), sodium hydroxide (NaOH), and hydrochloric acid (HCl) were obtained from Sinopharm Chemical Reagent Co., Ltd., (Shanghai, China).

### *2.2. Synthesis of $ZnIn_2S_4$/UiO-66-$NH_2$ Composites*

UiO-66-$NH_2$ nanoparticles were synthesized referring to the earlier reported literature [24]. $ZrCl_4$ (0.5 mmol) and 2-aminoterephthalic acid (0.5 mmol) were dissolved in DMF (80 mL) and stirred until clear then poured into 100 mL Teflon reactor. After heating for 48 h at 120 °C, the precipitate was collected and washed with DMF and finally dried under vacuum for 12 h at 50 °C. The UiO-66-$NH_2$ nanoparticles were obtained. The preparation of $ZnIn_2S_4$/UiO-66-$NH_2$ composites used a simple hydrothermal method [25]. Typically, a certain amount (0.01, 0.03, 0.05, and 0.1 mmol) of UiO-66-$NH_2$ was dispersed by ultrasound for 30 min in a mixed solution containing 15 mL ethylene glycol and 45 mL deionized water. Afterwards, 1 mmol Zn $(NO_3)_2 \cdot 6H_2O$, 2 mmol In $(NO_3)_3 \cdot xH_2O$, and 4 mmol thioacetamide were added to the dispersion continuously. The mixture was stirred for 2 h and then transferred into Teflon reactor (100 mL) for heating for 12 h at 160 °C. Finally, the suspension was centrifuged, washed with ethanol, and dried overnight to obtain the target solid

powder. The as-prepared samples were denoted as ZIS-UiO-*x*% (ZIS-UiO-1%, ZIS-UiO-3%, ZIS-UiO-5%, and ZIS-UiO-10%), where *x*% referred to the mass ratio of UiO-66-$NH_2$ to $ZnIn_2S_4$. The synthesis procedure is schematically depicted in Scheme 1, with the products of each reaction step being presented.




**Scheme 1.** Schematic synthesis of the ternary composite photocatalyst.

### *2.3. Fabrication of the Modified Electrode*

The preparation of $ZnIn_2S_4$/UiO-66-$NH_2$ modified electrode is as follows: 2 mg $ZnIn_2S_4$/UiO-66-$NH_2$ powders was dispersed in 1 mL water/ethanol ($V_{water}$:$V_{ethanol}$ = 1) mixture containing 20 μL Nafion. Then, the targeted modified electrode was fabricated in the following way: 5 μL dispersion was coated on a cleaned glassy carbon electrode (GCE, diameter 3.0 mm) and naturally dried.

### *2.4. Characterization and Analytical Measurements*

The surface morphology of the prepared samples was recorded by scanning electronic microscopy (SEM, Zeiss Sigma 300, Carl Zeiss Jena, Oberkochen, Germany), transmission electron microscopy (TEM, FEI Talos F200S, Thermo Fisher Scientific, Waltham, MA, USA), and high-resolution transmission electron microscopy (HRTEM, FEI Talos F200S, Thermo Fisher Scientific, Waltham, MA, USA). X-ray powder diffraction (XRD) data of the crystal structure of samples were obtained using an X-ray diffractor (D8 Advance, Bruker, Bremen, Germany) of D2 PHASER model with Cu Kα radiation and X-ray power of 30 kV/20 mA. Fourier transform infrared spectroscopy (FT-IR, Nicolet 6700, Thermo Fisher Scientific, Waltham, MA, USA) was applied to investigate the chemical structure. X-ray photoelectron spectroscopy (XPS, ESCALab220i-XL, VG Scientific, UK) was carried out to test the elemental states. $N_2$ adsorption-desorption experiments (BET, Autosorb-IQ-MP, Quantachrome, Boynton Beach, FL, USA) were performed to measure the specific surface area and pore size distribution. Before the $N_2$ adsorption measurement, the samples were degassed at 70 °C for 12 h.

All electrochemical experiments were carried out using a Shanghai Chenhua Instrumental Co., Ltd. (Shanghai, China) electrochemical workstation with a conventional three-electrode system. The $ZnIn_2S_4$/UiO-66-$NH_2$ modified electrode, the Pt wire (length 5 cm), and the Ag/AgCl electrode served as work electrode, auxiliary electrode, and reference electrode, respectively. The reference solution was saturated KCl solution. Cyclic voltammetry (CV) and differential pulse voltammetry (DPV) were used to investigate electrochemical characteristics. Moreover, 0.1 mol/L phosphate buffered solution (PBS),

with various pH values adjusted with HCl and NaOH, was employed as the supporting electrolyte in the succeeding experiments.

The xanthine (XA) and hypoxanthine (HXA) compound were determined by a modified method of Burns and Ke. Briefly, 1 g of muscle was homogenized with 5% cold perchloric acid [21]. The pH of the extract was adjusted to 6.4 with KOH and a final volume to 10 mL. The fractional quantities of xanthine (XA) and hypoxanthine (HXA) from a single sample were determined by using high-performance liquid chromatography with a Shim-pack column (6.0 mm diameter × 15 cm, 10 µm; Shimadzu, Kyoto, Japan). The UV-vis detector was set at 273 nm. The mobile phase was an acetonitrile/water mixture (25/75, $v/v$) at a flow rate of 1.5 mL·min$^{-1}$, while the injection volume was 5 mL·min$^{-1}$.

### *2.5. Pretreatment of Real Fish Sample*

The fish samples were taken from a fresh large yellow croaker living in the East China Sea (292.67 g; the dead large yellow croaker was subsequently stored at −4 °C). Before analysis, we needed to carry out the preprocessing operation on fish every day. Generally, 1 g fish meat was dissolved with 5% PCA solution then centrifuged and filtered several times to obtain the clarified supernatant in which the solution pH was stabilized at 6.4 with 1% KOH; eventually the supernatant was refrigerated at −20 °C as the follow-up sample concentrate.

## 3. Results and Discussion

XRD was used to identify the crystal structure of samples (Figure 1A). All diffraction peaks at XRD pattern of pure $ZnIn_2S_4$ are well matched to (006), (102), (104), (108), (110), (116), and (202) planes of hexagonal $ZnIn_2S_4$ (JCPDS No.65-2023) [26]. UiO-66-$NH_2$ was also prepared successfully, because these basic diffraction peaks appearing in UiO-66-$NH_2$ are the same as ones reported in literature [24]. For ZIS-UiO-$x$%, the XRD patterns have almost no changes, validating that the crystal structure of $ZnIn_2S_4$ is not destroyed after the introduction of UiO-66-$NH_2$. It can be observed from the insert of Figure 1A that a faint weak signal emerges at 2$\theta$ value of 7.3° in ZIS-UiO-10%, and it is the expression of UiO-66-$NH_2$ in the hybrids. In addition, to further study the composition of $ZnIn_2S_4$/UiO-66-$NH_2$, the FT-IR spectra of the synthesized samples were measured. As shown in Figure 1B, the faintish peaks found over $ZnIn_2S_4$ are ascribed to the physical absorption of water molecules and hydroxyl groups [27]. For pristine UiO-66-$NH_2$, the strong absorption peaks at 1569 cm$^{-1}$, 1427 cm$^{-1}$, and 1385 cm$^{-1}$ correspond to C–O–O symmetric stretching vibration, and the peak at 1652 cm$^{-1}$ belongs to the characteristic C=O stretching of carboxylate groups. The weak band at 1506 cm$^{-1}$ is identified as the C=C of a benzene ring. The relatively weaker characteristic vibration derived from O–Zr–O vibration in UiO-66-$NH_2$ results in the peaks at 764 cm$^{-1}$, 675 cm$^{-1}$, and 568 cm$^{-1}$ [25]. The FT-IR spectra of ZIS-UiO-$x$% are almost composed of absorption bands, ascribed to the UiO-66-$NH_2$ and $ZnIn_2S_4$ compounds, indicating the successful production of the binary composite. There are new absorption bands emerging in FT-IR spectra of ZIS-UiO-$x$%, and the strength increases with the increase of loading amount. By analysis, the XRD and FT-IR results all verify the successful synthesis of composites.

XPS was conducted to further analyze the elemental composition and chemical state of samples. As seen in the survey spectrum (Figure 1C), the composite (blue curve) recombined with $ZnIn_2S_4$ and UiO-66-$NH_2$ appears to have all of the characterized elements, even if the proportion of UiO-66-$NH_2$ is only 5%. In development, Figure 1D exhibits the high-resolution XPS spectra for Zr 3d of ZIS-UiO-5%, and the peaks centered at 183.1 eV and 185.41 eV correspond to Zr $3d_{5/2}$ and Zr $3d_{3/2}$, respectively, largely due to the presence of UiO-66-$NH_2$. As seen in Figure S1A, the high-resolution spectra of O1s could be deconvoluted into two peaks at 531.8 eV and 533.4 eV, attributed to Zr–O and C=O functional groups, respectively [28]. In addition, the peaks at 1021.7 eV (Zn $2p_{3/2}$) and 1044.7 eV (Zn $2p_{1/2}$) represent $Zn^{3+}$ (Figure S1B) of $ZnIn_2S_4$. The peaks at 444.8 eV

(In $2p_{5/2}$) and 452.3 eV (In $2p_{3/2}$) belong to $In^{3+}$ (Figure S1C). The peaks of S 2p at 161.6 eV and 162.8 eV (Figure S1D) are attributed to S $2p_{3/2}$ and S $2p_{1/2}$, respectively [28].

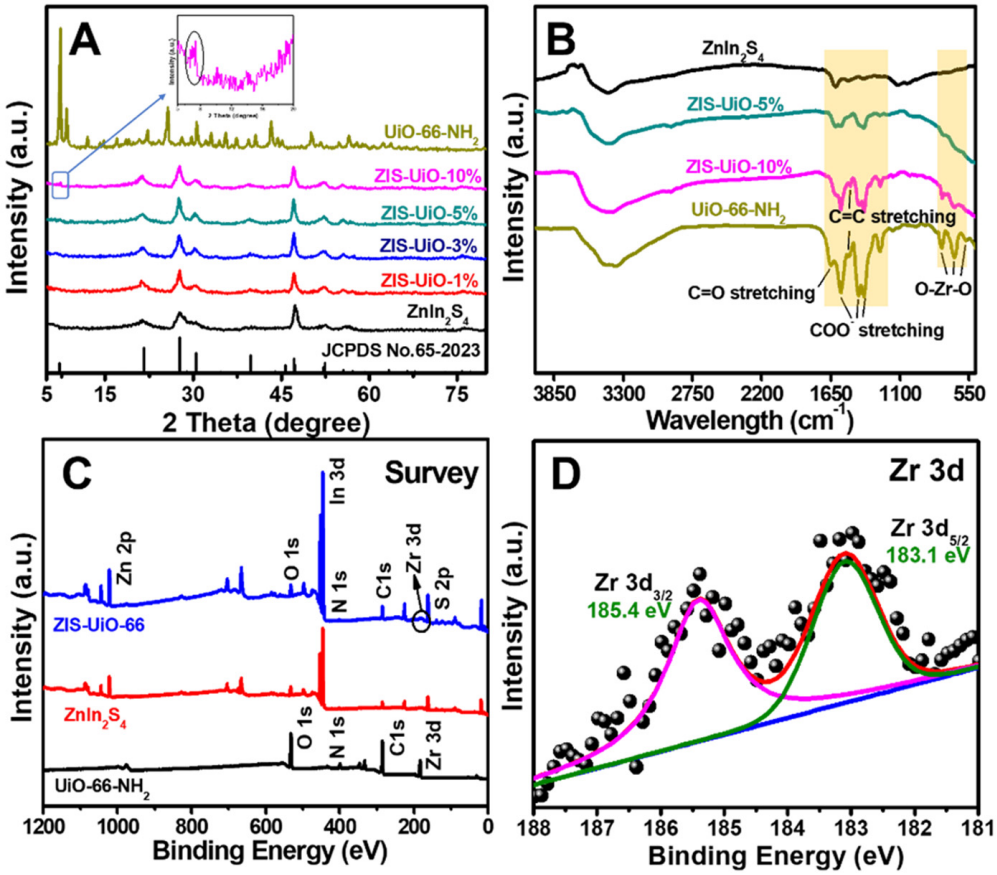



**Figure 1.** XRD patterns (**A**) and FT-IR spectra (**B**) of samples. XPS survey spectrum (**C**) of samples and high-resolution XPS spectra for Zr 3d (**D**) of ZIS-UiO-5%.

Figure 2 presents the surface microtopography of UiO-66-$NH_2$, $ZnIn_2S_4$, and ZIS-UiO-5% via SEM and TEM. By observing Figure 2A,D, the synthetic UiO-66-$NH_2$ are comparatively uniform octahedral particles. From Figure 2B,E, the pure $ZnIn_2S_4$ showed a clean flowerlike microsphere appearance which was composed of many thin nanosheets. The average diameter of microspheres is 5 μm. For as-synthesized ZIS-UiO-5%, we can find that the flowerlike morphology is almost stable, yet there are tiny particles attached to the surface, as shown in Figure 2C,F. The EDS spectrum (Figure 2G) also certifies the presence of Zr, O, Zn, In, and S elements in ZIS-UiO-5%. All of these images prove that samples are well formed and, importantly, the intimate contact is well formed between UiO-66-$NH_2$ and $ZnIn_2S_4$ in ZIS-UiO-5% composite, which may benefit charge transfer and further render superior electrochemical performance.

Subsequently, a low-temperature $N_2$ adsorption experiment was performed to measure the surface area ($S_{BET}$) and pore size distribution of samples. As displayed in Figure S2A, the type I (green curve) $N_2$ adsorption-desorption isotherm, in which the adsorption capacity increases rapidly at a lower relative pressure, belongs to UiO-66-$NH_2$, and there are micropores in this material. Pure $ZnIn_2S_4$ exhibits the type IV isotherm with an H3 hysteresis loop, corresponding to a system of capillary condensation of porous adsorbent. The isotherm of ZIS-UiO-5% shows a combined characteristic of type I/IV isotherms, indicating that the micropores and mesopores coexist in this composite. Meanwhile, the computed results (Table S1) attest that the hybrid has superior $S_{BET}$ and pore structure compared with pure $ZnIn_2S_4$. Superior $S_{BET}$ means abundant active sites, signifying favorable electrochemical properties [25]. Besides, the electrochemical behavior

of $ZnIn_2S_4$, ZIS-UiO-1%, ZIS-UiO-3%, ZIS-UiO-5%, and ZIS-UiO-10% was evaluated in 2.5 mM $[Fe(CN)_6]^{3-/4-}$ and 0.1 M KCl by varying scan rates over 25–300 mV/s, and one of the CV profiles is depicted in Figure S2B. According to the Randles–Sevick equation [29]: $I_p = 2.65 \times 10^5 n^{3/2} A D^{1/2} v^{1/2} C_0$, in which $n$ = 1 (electron transfer numbers) and $D = 7.6 \times 10^{-6}$ $cm^2/s$ (diffusion coefficient), the electrochemical surface area of ZIS-UiO-5% is calculated to be 0.139 $cm^2$, higher than others and approximately 2.6 times as large as that of $ZnIn_2S_4$ (Table S2). The obtained conclusion implies that the addition of UiO-66-$NH_2$ nanoparticles could increase the active surface areas and, therefore, enhance the current signals.

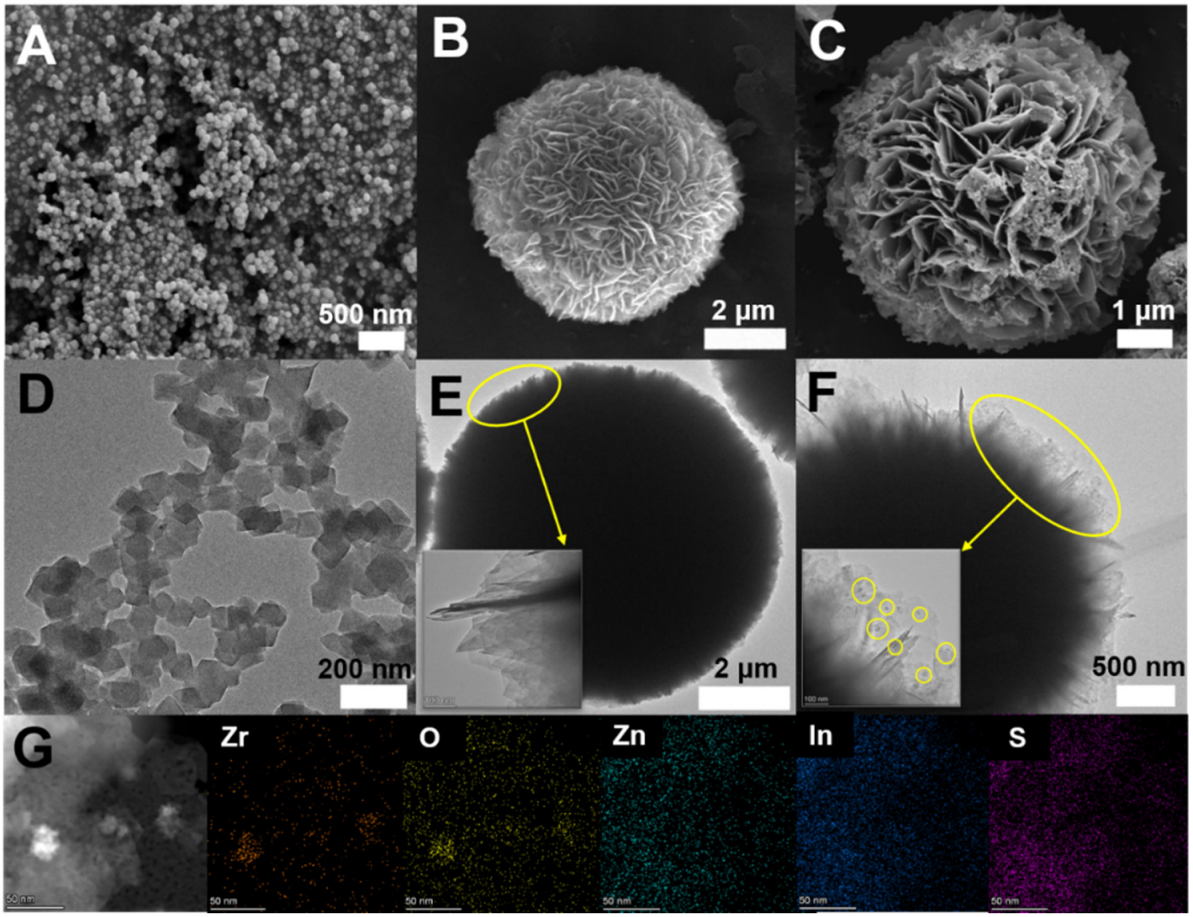



**Figure 2.** SEM (**A**–**C**), TEM (**D**,**E**) images of UiO-66-$NH_2$ (**A**,**D**), $ZnIn_2S_4$ (**B**,**E**), and ZIS-UiO-5% (**C**,**F**), and EDX spectrum (**G**) of ZIS-UiO-5%.

In the first place, the CV method was utilized to detect whether the modified electrode responded to XA and HXA individually, as presented in Figure 3A. Obviously, it is unresponsive in the absence of XA or HXA in PBS. As 5 μM XA is put into buffered solution, a distinct peak becomes visible in this CV curve at a potential of 0.75 V, attributed to XA. By the same operation, the electrode could be verified to have a correct response to HXA. It is proved that this modified electrode can react swiftly to target substances. Then DPV was employed to examine the electrochemical performance of XA and HXA simultaneously. Figure 3B shows the DPVs of different modified electrodes in PBS containing 5 μM XA and 10 μM HXA. One can see that as-prepared electrodes have decent current responses to both HXA and XA, and the electrode modified by composite material has a better response compared to pristine materials. This conclusion demonstrates that the introduction of UiO-66-$NH_2$ does have a positive effect on detecting XA and HXA. Moreover, tests of the influence of UiO-66-$NH_2$ content on detection were carried out. As shown in Figure 3C, the current response first increased and then decreased, and the maximum appears when

the UiO-66-$NH_2$ content is 5%. Besides, the influence of deposition time also cannot be ignored. As depicted in Figure 3D, the longer the deposition time, the larger the current density, and the peak current reaches the highest value at 90 s then falls and flattens out. It turns out that accumulation over time can improve the current signal, until the electrode surface becomes saturated. Thence, subsequent DPV experiments were performed with ZIS-UiO-5% modified electrode under deposition time of 90 s.

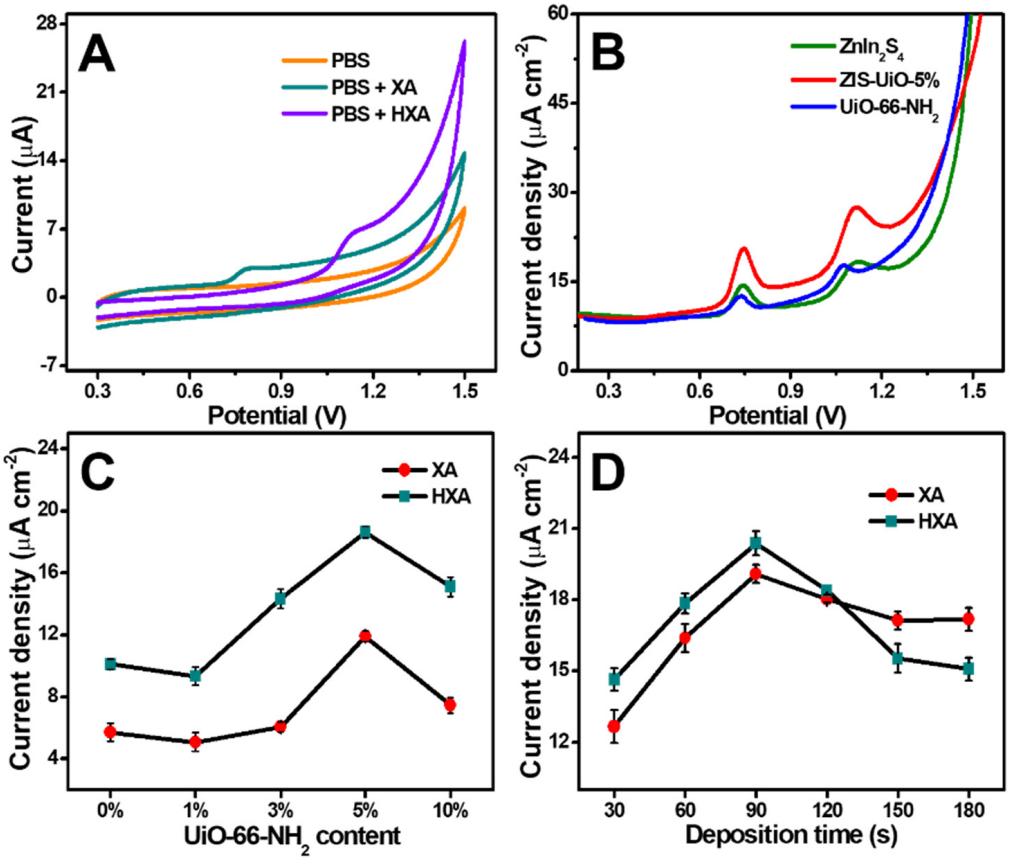



**Figure 3.** CV profiles (**A**) of ZIS−UiO −5% in PBS (pH 6.0) with/without XA or HXA. DPV curves (**B**) of different samples in PBS (pH 6.0) containing 5 μM XA and 10 μM HXA. Effects of UiO-66-$NH_2$ content in composite (**C**) and deposition time of ZIS−UiO −5% modified electrode (**D**) to HXA and XA detection in PBS (pH 6.0) containing 5 μM XA and 10 μM HXA.

Considering the influence of PBS pH effect on detecting XA and HXA, a set of PBS solutions with different pH values was investigated. Figure S3A,B illustrate that the $\Delta I$ decreases after the summit at pH 6.0, ranging from 5.5 to 8.5, and the linear relations of the oxidation potential ($E_p$) and pH, as presented in Figure S3C, can be expressed as: $E_p$ (XA) = −0.0636 pH + 1.1552 ($R^2$ = 0.9955) and $E_p$ (HXA) = −0.0634 pH + 1.5885 ($R^2$ = 0.9979). According to the literature [30], both obtained slopes are close to the expected value (57 mV per pH), indicating that the number of proton transfers and electron transfers are equal in the oxidations of XA and HXA. What happened then was the investigation of reaction kinetics on the electrode surface, which was measured applying CV by varying scan rates (125–300 mV/s). In the presence of 5 μM XA and 10 μM HXA (PBS, pH 6.0), the peak currents increase gradually, and the oxidation potentials are positively shifted distinctly in the wake of the scan rate increment (Figure S3D–F). It can be speculated that both electrochemical oxidation processes are diffusion-controlled ($\Delta I$ is proportional to $v^{1/2}$) and irreversible. The relationship of log$v$ vs. $E_p$ can be given by the Laviron equation: $E_p = E^\theta + (2.303RT/\alpha nF)\log(RTk^\theta/\alpha nF) + (2.303RT/\alpha nF)\log v$ and, combined with the Bard and Faulkner equation: $\alpha = 47.7/(E_p - E_{p/2})$, where $E_{p/2}$ represents the potential at which the current is half of the peak value. The transfer electron numbers could be

calculated as $n$ (XA) = 2.08 ≈ 2 and $n$ (HXA) = 2.11 ≈ 2, respectively. To sum up, both oxidations involve two electron transfers, and the process can be sketched as Scheme S1.

Under the best detection condition (obtained in the above experiments), DPV, which is provided with higher sensitivity and better resolution than other methods, was employed for the simultaneous determination of XA and HXA. Figure 4A shows the DPVs of different XA concentrations containing 5 μM HXA, and the peak current of XA increases linearly, ranging from 0.025 to 20 μM. The corresponding equation of linear regression is $\Delta I$ = 1.504 $C_{XA}$ (μM) + 2.646 ($R^2$ = 0.9985) (Figure 4B). The DPV profiles which present the current density increase over the HXA concentration range of 0.3–25 μM containing fixed 5 μM XA were illustrated in Figure 4C,D. The linear equation is fitted to $\Delta I$ = 1.195 $C_{HXA}$ (μM) + 3.48 ($R^2$ = 0.9990). Furthermore, the experiment of simultaneously increasing concentrations of XA (0.025–40 μM) and HXA (0.3–40 μM) (PBS, pH 6.0) was carried out (see Figure 4E). It could be observed that both peak current values rise linearly with their concentrations (Figure 4F). The result demonstrates that the as-prepared modified electrode can determine XA and HXA without interference. The two regression curves could be received: $\Delta I$ = 1.732 $C_{XA}$ (μM) + 3.016 ($R^2$ = 0.9989) and $\Delta I$ = 0.957 $C_{HXA}$ (μM) + 4.297 ($R^2$ = 0.9992). The limit of detections (LOD, S/N = 3) are 0.0083 μM and 0.1 μM, respectively, and the obtained LOD values in this work are comparable to and even better than those reported previously (Table S3).

The reproducibility and stability of detecting XA and HXA simultaneously for as-prepared ZIS-UiO-5% modified electrode was evaluated under optimized conditions. As shown in Figure S4A, the current densities of both determinants just decrease less (about 2.33% for XA and 3.16% for HXA) after multiple cycles compared to the first cycle, and the relative standard deviations (RSD) are 1.39% (XA) and 1.91% (HXA). The periodic stability tested in Figure S4B, exhibiting the RSDs of XA and HXA, are 3.89% and 3.21%. Additionally, to exclude the influence of the electrode itself on the experiment, we used five electrodes to perform the same test under the same test environment. As shown in Figure S4C, there is almost no effect, and the RSDs are 1.03% (XA) and 1.09% (HXA). These results can demonstrate that the ZIS-UiO-5% modified electrode possesses outstanding reproducibility and stability. Interference identification was investigated in mixed solution (XA + HXA) containing several interfering compounds, such as glucose, p-acetamidophenol, folic acid, citric acid, ascorbic acid, uric acid, $Na^+$, $Cl^-$, and $SO_4^{2-}$ (Figure S4D,E). Outcomes prove that 10-times organics and 20-times excess of inorganic compounds both have a low effect on XA and HXA detection, meaning that the anti-interference performance of this electrode is excellent. As shown in Scheme S2, one can observe a selective schematic diagram of XA and HXA. Due to the presence of UiO-66-$NH_2$, the modified electrode material improves the adsorption of XA and HXA, but the oxidation process of XA and HXA on the sensor platform is selective. HAX loses electrons and hydrogen ions in the presence of water to form AX. After electron transfer through the sensor platform, AX loses electrons and hydrogen ions in the presence of water to further form UA.

The practical application of this selected ZIS-UiO-5% modified electrode was further established by detecting XA and HXA in fish. The concentrated solution (1 g of muscle was homogenized with 5% cold perchloric acid; the pH of the extract was adjusted to 6.4 with KOH and a final volume to 10 mL) was diluted five times with PBS (pH 6.0) as an electrochemical test solution, and the marked recovery method was conducted by adding an amount of known XA and HXA into the fish meat samples to verify the practicability of the developed sensing platform. As exhibited in Table 1, the recovery rates of the spiked samples are 96–103% for XA and 97–101% for HXA, with RSD of 1.35–2.86%, which confirmed that this method could well apply to detecting XA and HXA in fish meat samples without interference of sample matrix. Besides, for attesting to the accuracy of this sensor, a 10.0 μL sample solution was also used for HPLC analysis and compared with the electrochemical monitoring results for the contents of HXA in fish meat within six days [31]. From Table 2, we can clearly find that the results agree with each other, and the relative errors are controlled within 6%, indicating that this designed sensor has good accuracy.

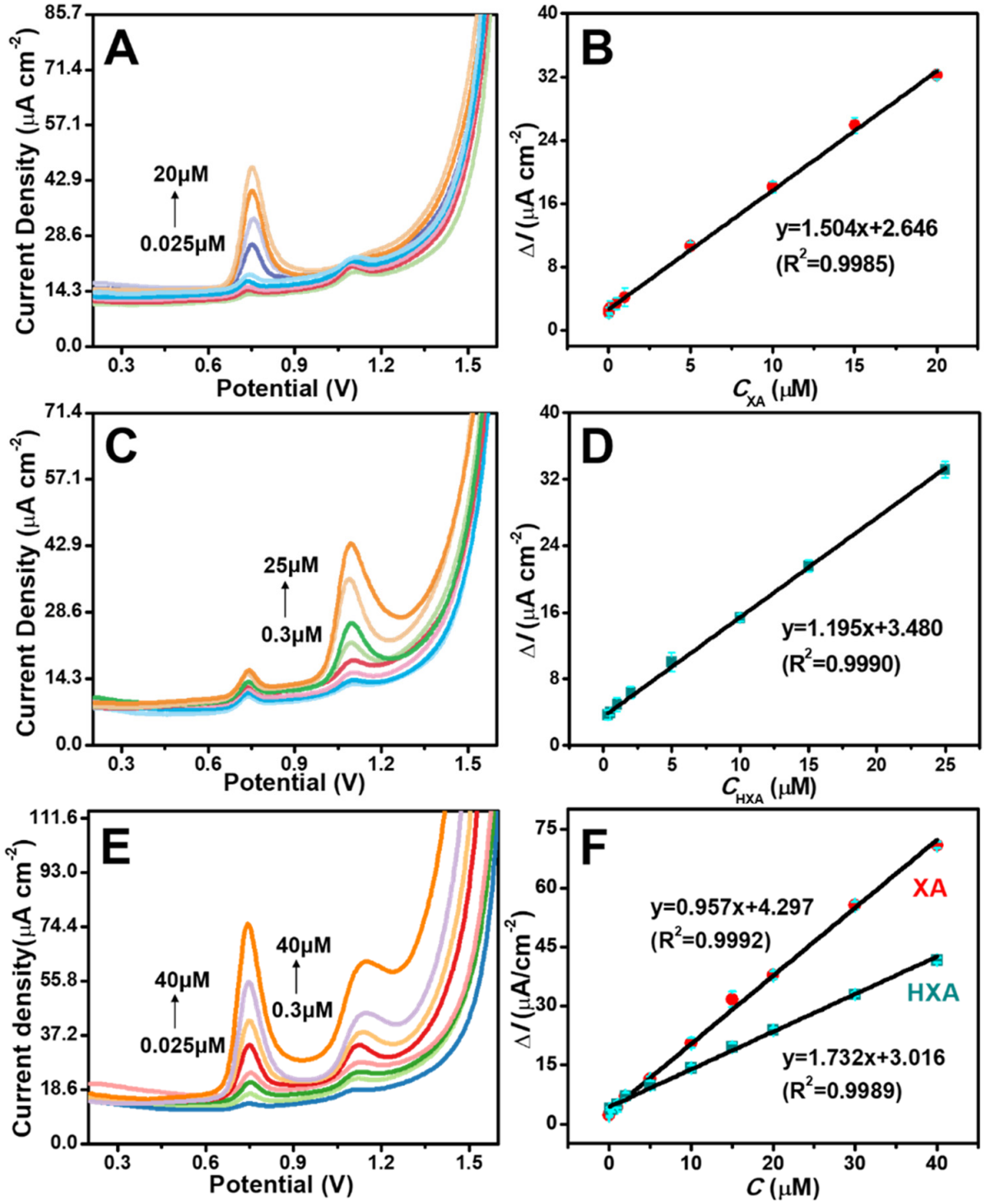



**Figure 4.** DPV curves (**A**) in PBS of different XA concentration (0.025, 0.05, 0.1, 0.3, 0.5, 1, 2, 5, 10, and 20 μM) with 5 μM HXA at ZIS-UiO-5% and corresponding fitted line (**B**) of Δ*I* vs. $C_{XA}$ (μM). DPV curves (**C**) in PBS of different HXA concentration (0.3, 0.5, 1, 2.5, 5, 10, 15, and 25 μM) with 5 μM XA at ZIS-UiO-5% and corresponding fitted line (**D**) of Δ*I* vs. $C_{HXA}$ (μM). DPV curves (**E**) in PBS of different HXA concentration (0.025, 1, 5, 10, 15, 20, 30, and 40 μM) and different XA concentration (0.3, 2.5, 5, 10, 15, 20, 30, and 40 μM) at ZIS-UiO-5% and corresponding fitted line (**F**) of Δ*I* vs. *C* (μM).

**Table 1.** Determination of XA and HXA in fish meat.

| Real Samples | Analyte | Added (μM) | Found (μM) | RSD (%) | Recovery (%) |
|---|---|---|---|---|---|
| Fish meat | XA | 0.00 | 1.22 | 2.86 | / |
| | | 2.00 | 3.20 | 2.03 | 99.42 |
| | | 4.00 | 5.01 | 1.35 | 96.87 |
| | | 6.00 | 6.37 | 1.21 | 102.41 |
| | HXA | 0.00 | 6.60 | 2.76 | / |
| | | 5.00 | 11.58 | 2.30 | 99.76 |
| | | 10.00 | 16.21 | 1.92 | 97.69 |
| | | 15.00 | 21.76 | 1.53ł | 100.72 |

**Table 2.** Contents of HXA in fish meat at different times.

| Time (Day) | HXA (μM) | | Relative Error (%) |
|---|---|---|---|
| | ZIS−UiO−5%-GCE | HPLC | |
| 1 | 15.10 | 15.23 | −0.90 |
| 2 | 29.25 | 28.93 | 1.19 |
| 3 | 31.30 | 33.45 | −6.46 |
| 4 | 44.65 | 43.12 | 3.55 |
| 5 | 71.95 | 68.23 | 5.48 |
| 6 | 81.00 | 86.21 | 6.00 |

## 4. Conclusions

Herein, the $ZnIn_2S_4$/UiO-66-$NH_2$ composite which was prepared via a plain solvothermal method was proposed to construct an electrochemical sensing platform for XA and HXA. This binary system demonstrated high selectivity and sensitivity to XA and HXA individually and simultaneously, along with low detection limit and wide linear range. Besides, $ZnIn_2S_4$/UiO-66-$NH_2$ also behaved well in real fish meat samples with good recovery rates. As proved by facts, the fabricated sensor can be utilized in determination of fish freshness, and it will have a promising application in the food industry.

**Supplementary Materials:** The following supporting information can be downloaded at: https://www.mdpi.com/article/10.3390/chemosensors10050158/s1. Figure S1. High-resolution XPS spectra for Zn 2p (A), In 3d (B), S 2p (C), and O1s (D) of ZIS-UiO-5%. Figure S2. $N_2$ adsorption-desorption isotherms (A) of samples. CV profiles of the ZIS-UiO-5% modified GCEs measured at different scan rates (25, 50, 75, 100, 125, 150, 175, 200, 225, 250, 275, and 300 mV/s) in presence of 2.5 mM $[Fe(CN)_6]^{3-/4-}$ in 0.1 M KCl. The inset presents the fitted line of Δ*I* vs. v1/2 at ZIS-UiO-5%. Figure S3. DPV curves (A) of ZIS-UiO-5% modified electrode in PBS containing 10 μM HXA and 5 μM XA at different pH values (5.5–8.5). Plots of the peak current density (B) and the oxidation potential (C) vs. pH value. CV profiles (D) of ZIS-UiO-5% modified electrode in PBS (pH 6.0) with 10 μM HXA and 5 μM XA at various scan rates from 125 to 300 mV/s. The linear relationship of the peak current vs. v (E) and the peak potential vs. logv (F). Figure S4. DPV curves (A) of six tests in a row at one electrode in PBS (pH 6.0) with 5 μM XA and HXA. Repetitive measurements (B) of 5 μM XA and HXA at one electrode. Histogram (C) of reproducibility of 5 μM XA and HXA at five electrodes. Histogram (D, E) of selectivity at ZIS-UiO-5% modified electrode for XA (D) and HXA (E) (the analysis method is the same as the above DPV curve measurement method). Moreover, 0.1 mol/L PBS was used as the supporting electrolyte. The distractor is added when the electrolyte is configured. The distractors are 50 μM glucose, 50 μM p-acetamidophenol, 50 μM folic acid, 50 μM citric acid, 50 μM ascorbic acid, 50 μM uric acid, 0.1 mM $Na^+$, 0.1 mM $Cl^-$, and 0.1 mM $SO_4^{2-}$, respectively). Table S1. The values of $S_{BET}$ and pore volume of samples. Table S2. Electroactive surface area of samples. Scheme S1. The oxidation process of HXA and XA. Table S3. Comparison of reported different electrode modifiers for the XA and HXA determination [22,29,32–35]. Scheme S2. Selective schematic diagram of XA and HXA.

**Author Contributions:** Conceptualization, methodology, visualization, writing—original draft, writing—review and editing, Q.C.; methodology, data curation, funding acquisition, B.Z., P.Y.,

H.T. and C.Z.; data curation, validation, writing—review and editing, L.Z.; investigation, data curation, validation, visualization, D.S.; investigation, resources, funding acquisition, T.J. and Z.L.; investigation, resources, P.Y.; formal analysis, methodology, C.Z.; conceptualization, methodology, writing—review and editing, H.T.; design experiments, W.S. All authors have read and agreed to the published version of the manuscript.

**Funding:** This work was supported by the National Natural Science Foundation of China (No.22005269); the NSFC-Zhejiang Joint Fund for Integration of Industrialization and Diversification (U1809214); the National Natural Science Foundation of Zhejiang Province (LQ21B030007 and LQ22C200014); and the Science and Technological program of Ningbo (Grant 2021S136); Zhoushan science and technology project of China (2019C43276).

**Institutional Review Board Statement:** Not applicable.

**Informed Consent Statement:** Not applicable.

**Data Availability Statement:** The authors confirm that the data supporting the findings of this study are available within the article and its supplementary materials. The raw data generated at Zhejiang Ocean University are available on request from the corresponding author.

**Conflicts of Interest:** The authors declare that they have no known competing financial interests or personal relationships that could have appeared to influence the work reported in this paper.

## Abbreviations

4B-PGE (4B grade pencil graphite electrode); P6-TG/GCE (polymerized film of 6-thioguanine modified on glassy carbon electrode); rGO (reduced graphene oxide); CS (chitosan); B-CeO2NCs (B-doped $CeO_2$ nanocubes); GCPE (glassy carbon microspheres paste electrode).

## References

1. Chen, Z.T.; Lin, Y.; Ma, X.M.; Guo, L.H.; Qiu, B.; Chen, G.N.; Lin, Z.Y. Multicolor biosensor for fish freshness assessment with the naked eye. *Sens. Actuators B Chem.* **2017**, *252*, 201–208. [CrossRef]
2. Wu, D.; Zhang, M.; Chen, H.; Bhandari, B. Freshness monitoring technology of fish products in intelligent packaging. *Crit. Rev. Food Sci. Nutr.* **2020**, *61*, 1279–1292. [CrossRef] [PubMed]
3. Kassemsarn, B.O.; Perez, B.S.; Murray, J.; Jones, N. Nucleotide degradation in the muscle of iced haddock (Gadus aeglefinus), lemon sole (Pleuronectes microcephalus), and plaice (Pleuronectes platessa). *J. Food Sci.* **1963**, *28*, 28–37. [CrossRef]
4. Karube, I.; Matsuoka, H.; Suzuki, S.; Watanabe, E.; Toyama, K. Determination of fish freshness with an enzyme sensor system. *J. Agric. Food Chem.* **1984**, *32*, 314–319. [CrossRef]
5. Lawal, A.T.; Adeloju, S.B. Mediated xanthine oxidase potentiometric biosensors for hypoxanthine based on ferrocene carboxylic acid modified electrode. *Food Chem.* **2012**, *135*, 2982–2987. [CrossRef] [PubMed]
6. Mustafa, F.; Othman, A.; Andreescu, S. Cerium oxide-based hypoxanthine biosensor for Fish spoilage monitoring. *Sens. Actuators B Chem.* **2021**, *332*, 129435. [CrossRef]
7. Masuoka, N. Stilbene compounds are specific inhibitors of the superoxide anion generation catalyzed by xanthine oxidase. *Food Chem.* **2021**, *12*, 100146. [CrossRef]
8. Kuś, P.M.; Rola, R. LC-QqQ-MS/MS methodology for determination of purine and pyrimidine derivatives in unifloral honeys and application of chemometrics for their classification. *Food Chem.* **2021**, *348*, 129076. [CrossRef]
9. Pu, W.D.; Zhao, H.W.; Wu, L.P.; Zhao, X.Y. A colorimetric method for the determination of xanthine based on the aggregation of gold nanoparticles. *Microchim. Acta* **2015**, *182*, 395–400. [CrossRef]
10. Shan, D.; Wang, Y.N.; Zhu, M.J.; Xue, H.G.; Cosnier, S.; Wang, C.Y. Development of a high analytical performance-xanthine biosensor based on layered double hydroxides modified-electrode and investigation of the inhibitory effect by allopurinol. *Biosens. Bioelectron.* **2009**, *24*, 1171–1176. [CrossRef]
11. Lu, Z.W.; Zhong, J.; Zhang, Y.; Sun, M.M.; Zou, P.; Du, H.J.; Wang, X.X.; Rao, H.B.; Wang, Y.Y. MOF-derived $Co_3O_4/FeCo_2O_4$ incorporated porous biomass carbon: Simultaneous electrochemical determination of dopamine, acetaminophen and xanthine. *J. Alloys Compd.* **2021**, *858*, 157701. [CrossRef]
12. Pierini, G.D.; Robledo, S.N.; Zon, M.A.; Di Nezio, M.S.; Granero, A.M.; Fernández, H. Development of an electroanalytical method to control quality in fish samples based on an edge plane pyrolytic graphite electrode. Simultaneous determination of hypoxanthine, xanthine and uric acid. *Microchem. J.* **2018**, *138*, 58–64. [CrossRef]
13. Juárez-Gómez, J.; Ramírez-Silva, M.T.; Guzmán-Hernández, D.S.; Romero-Romo, M.; Palomar-Pardavé, M. Novel electrochemical method to evaluate the antioxidant capacity of infusions and beverages, based on in situ formation of free superoxide radicals. *Food Chem.* **2020**, *332*, 127409. [CrossRef] [PubMed]

14. Hoyos-Arbeláez, J.; Vázquez, M.; Contreras-Calderón, J. Electrochemical methods as a tool for determining the antioxidant capacity of food and beverages: A review. *Food Chem.* **2017**, *221*, 1371–1381. [CrossRef]
15. Hu, S.; Yu, Y.; Guan, Y.; Li, Y.; Wang, B.; Zhu, M. Two-dimensional $TiO_2$ (001) nanosheets as an effective photo-assisted recyclable sensor for the electrochemical detection of bisphenol A. *Chin. Chem. Lett.* **2020**, *31*, 2839–2842. [CrossRef]
16. Xi, J.J.; Wang, H.; Zhang, B.H.; Zhao, F.Q.; Zeng, B.Z. Novel molecularly imprinted photoelectrochemical sensor for rutin based on $Bi_2S_3/ZnIn_2S_4$ heterojunction. *Sens. Actuators B Chem.* **2020**, *320*, 128409. [CrossRef]
17. Ma, H.; Liu, Y.; Xiong, R.; Wei, J. Hetero-structured $ZnIn_2S_4$-NiO@MOF photo-catalysts for efficient hydrogen evolution. *Chin. Chem. Lett.* **2022**, *33*, 1042–1046. [CrossRef]
18. Pourtaheri, E.; Taher, M.A.; Ali, G.A.; Agarwal, S.; Gupta, V.K. Electrochemical detection of gliclazide and glibenclamide on $ZnIn_2S_4$ nanoparticles-modified carbon ionic liquid electrode. *J. Mol. Liq.* **2019**, *289*, 111141. [CrossRef]
19. Liu, S.Y.; Lai, C.; Liu, X.G.; Li, B.S.; Zhang, C.; Qin, L.; Huang, D.L.; Yi, H.; Zhang, M.M.; Li, L. Metal-organic frameworks and their derivatives as signal amplification elements for electrochemical sensing. *Coordin. Chem. Rev.* **2020**, *424*, 213520. [CrossRef]
20. Cruz-Navarro, J.A.; Hernandez-Garcia, F.; Romero, G.A.A. Novel applications of metal-organic frameworks (MOFs) as redox-active materials for elaboration of carbon-based electrodes with electroanalytical uses. *Coordin. Chem. Rev.* **2020**, *412*, 213263. [CrossRef]
21. Li, C.L.; Hao, J.X.; Wu, K.B. Triethylamine-controlled Cu-BTC frameworks for electrochemical sensing fish freshness. *Anal. Chim. Acta* **2019**, *1085*, 68–74. [CrossRef] [PubMed]
22. Zhang, L.; Li, S.B.; Xin, J.J.; Ma, H.Y.; Pang, H.J.; Tan, L.C.; Wang, X.M. A non-enzymatic voltammetric xanthine sensor based on the use of platinum nanoparticles loaded with a metal-organic framework of type MIL-101 (Cr). Application to simultaneous detection of dopamine, uric acid, xanthine and hypoxanthine. *Microchim. Acta* **2019**, *186*, 1–10. [CrossRef] [PubMed]
23. Zhang, X.; Yang, Y.; Qin, P.; Han, L.; Zhu, W.; Duan, S.; Lu, M.; Cai, Z. Facile preparation of nano-g-$C_3N_4$/UiO-66-$NH_2$ composite as sorbent for high-efficient extraction and preconcentration of food colorants prior to HPLC analysis. *Chin. Chem. Lett.* **2022**, *33*, 903–906. [CrossRef]
24. He, B.; Dong, X. Hierarchically porous Zr-MOFs labelled methylene blue as signal tags for electrochemical patulin aptasensor based on ZnO nano flower. *Sens. Actuators B Chem.* **2019**, *294*, 192–198. [CrossRef]
25. Yang, J.; He, X.Q.; Dai, J.; Tian, R.; Yuan, D.S. Photo-assisted enhancement performance for rapid detoxification of chemical warfare agent simulants over versatile $ZnIn_2S_4$/UiO-66-$NH_2$ nanocomposite catalysts. *J. Hazard. Mater.* **2021**, *417*, 126056. [CrossRef] [PubMed]
26. Ye, H.L.; Wang, H.; Zhang, B.H.; Zhao, F.Q.; Zeng, B.Z. Tremella-like $ZnIn_2S_4$/graphene composite based photoelectrochemical sensor for sensitive detection of dopamine. *Talanta* **2018**, *186*, 459–466. [CrossRef] [PubMed]
27. Chen, Q.W.; Yuan, C.; Zhai, C.Y. Label-free photoelectrochemical sensor based on 2D/2D $ZnIn_2S_4$/g-$C_3N_4$ heterojunction for the efficient and sensitive detection of bisphenol A. *Chin. Chem. Lett.* **2021**, *33*, 983–986. [CrossRef]
28. Liu, B.B.; Liu, X.J.; Liu, J.Y.; Feng, C.J.; Li, Z.; Li, C.; Gong, Y.Y.; Pan, L.K.; Xu, S.Q.; Sun, C.Q. Efficient charge separation between UiO-66 and $ZnIn_2S_4$ flowerlike 3D microspheres for photoelectronchemical properties. *Appl. Catal. B Environ.* **2018**, *226*, 234–241. [CrossRef]
29. Ibrahim, H.; Temerk, Y. A novel electrochemical sensor based on B doped $CeO_2$ nanocubes modified glassy carbon microspheres paste electrode for individual and simultaneous determination of xanthine and hypoxanthine. *Sens. Actuators B Chem.* **2016**, *232*, 125–137. [CrossRef]
30. Zhou, Y.Z.; Yang, L.H.; Li, S.H.; Dang, Y. A novel electrochemical sensor for highly sensitive detection of bisphenol A based on the hydrothermal synthesized Na-doped $WO_3$ nanorods. *Sens. Actuators B Chem.* **2017**, *245*, 238–246. [CrossRef]
31. Hoan, N.; Minh, N.; Trang, N.; Thuy, L.; Hoang, C.; Mau, T.; Vu, H.X.; Thu, P.; Phong, N.; Khieu, D. Simultaneous voltammetric determination of uric acid, xanthine, and hypoxanthine using $CoFe_2O_4$/reduced graphene oxide-modified electrode. *J. Nanomater.* **2020**, *2020*, 9797509. [CrossRef]
32. Vishnu, N.; Gandhi, M.; Rajagopal, D.; Kumar, A.S. Pencil graphite as an elegant electrochemical sensor for separation-free and simultaneous sensing of hypoxanthine, xanthine and uric acid in fish samples. *Anal. Methods* **2017**, *9*, 2265–2274. [CrossRef]
33. Lan, D.X.; Zhang, L. Electrochemical synthesis of a novel purine-based polymer and its use for the simultaneous determina-tion of dopamine, uric acid, xanthine and hypoxanthine. *J. Electroanal. Chem.* **2015**, *757*, 107–115. [CrossRef]
34. Ghanbari, K.; Nejabati, F. Ternary nanocomposite-based reduced graphene oxide/chitosan/$Cr_2O_3$ for the simultaneous determination of dopamine, uric acid, xanthine, and hypoxanthine in fish meat. *Anal. Methods* **2020**, *12*, 1650–1661. [CrossRef]
35. Durai, L.; Badhulika, S. Facile synthesis of large area pebble-like β-$NaFeO_2$ perovskite for simultaneous sensing of dopamine, uric acid, xanthine and hypoxanthine in human blood. *Mat. Sci. Eng. C* **2020**, *109*, 110631. [CrossRef]